Effects of shielding gas compositions on arc plasma and metal transfer in gas metal arc welding

Z. H. Rao,[1,2] S. M. Liao,[1] and H. L. Tsai[2,a)]
[1]*School of Energy Science and Engineering, Central South University, Changsha 410083, People's Republic of China*
[2]*Department of Mechanical and Aerospace Engineering, Missouri University of Science and Technology, Rolla, Missouri 65409, USA*

(Received 6 October 2009; accepted 14 December 2009; published online 22 February 2010)

This article presents the effects of shielding gas compositions on the transient transport phenomena, including the distributions of temperature, flow velocity, current density, and electromagnetic force in the arc and the metal, and arc pressure in gas metal arc welding of mild steel at a constant current input. The shielding gas considered includes pure argon, 75% Ar, 50% Ar, and 25% Ar with the balance of helium. It is found that the shielding gas composition has significant influences on the arc characteristics; droplet formation, detachment, transfer, and impingement onto the workpiece; and weld pool dynamics and weld bead profile. As helium increases in the shielding gas, the droplet size increases but the droplet detachment frequency decreases. For helium-rich gases, the current converges at the workpiece with a "ring" shape which produces non-Gaussian-like distributions of arc pressure and temperature along the workpiece surface. Detailed explanations to the physics of the very complex but interesting transport phenomena are given. © *2010 American Institute of Physics*. [doi:10.1063/1.3291121]

I. INTRODUCTION

In gas metal arc welding (GMAW), shielding gas is necessary not only to provide a protective environment for the molten metal but also can influence arc characteristics, mode of metal transfer, weld bead shape, and weld penetration.[1] In other words, the shielding gas composition has pronounced effects on the efficiency, quality, and overall performance of the welding operation. In recent years, the selection of shielding gas for achieving better welding performance has been extensively studied through the trial-and-error procedure,[2–8] and an increasing range of shielding gas has been available to achieve stable plasma arc, smooth metal transfer, and reduced weld defects.

Argon is the most common shielding gas used in GMAW. As an inert gas, argon does not react with molten metal, which also has a better arc starting and arc stability due to its low ionization potential (15.75 V). Like argon, helium is also a chemically inert gas. With a high ionization potential (24.58 V), however, a much higher arc voltage is required to ionize helium, thus producing a higher arc energy density.[1] Helium is more expensive than argon. Therefore, helium is often mixed with various percentages of argon to obtain the advantages of each individual gas. It has been reported[8–11] that shielding gas compositions significantly affect the metal transfer mode. In GMAW, metal is transferred from the electrode tip to the workpiece by three basic modes: short-circuit transfer, globular transfer, or spray transfer. Globular mode involves a droplet with larger diameter than that of the electrode and a transfer rate of a few droplets per second. Above the transition current, the metal transfer changes to spray mode that is characterized by very small droplets and an extremely high detachment frequency. In argon shielding, there is a sharp increase in droplet detachment frequency and decrease in droplet size when the metal transfer mode changes from globular to spray.[8–10] However, for helium arc welding, Rhee and Kannatey-Asibu[8] observed that metal transfer normally occurs in globular mode at any usable current level, and the droplet frequency is much less than that for argon. Apparently, the shielding gas composition has significant effects on arc plasma and metal transfer.

As GMAW involves nontransparent metal and very high temperature and high velocity arc plasma, it is very difficult, if not impossible to understand the underlying physics and the interplay among many process parameters through experiments. The trial-and-error experimental procedure is time consuming and costly. Hence, mathematical modeling provides a convenient way to study and understand the physical phenomena involved in GMAW. Generally, a comprehensive model for the GMAW process includes the following three events: (1) the generation and evolution of arc plasma, (2) the dynamic process of electrode melting, droplet formation, detachment, and impingement into the weld pool, and (3) the dynamics of weld pool and bead formation. However, due to complexity, most of the published models[12–19] only focused on one or two of these events while simplifying the rest of the events. Recently, Hu and Tsai[20,21] developed a real unified mathematical model employing the volume of fluid (VOF) technique and the continuum formulation to simulate the complete GMAW process with interactive coupling of all the three events. In their study, however, only pure argon was used as shielding gas, and the influences of shielding gas compositions on arc plasma and metal transfer were not included.

Very few models[22–24] have been developed to study the

a)Author to whom correspondence should be addressed. Electronic mail: tsai@mst.edu.

effect of shielding gas compositions in GMAW. Nemchinsky[22] developed a simple steady model to study the influence of various shielding gases on metal transfer. Haidar and Lowke[23] numerically studied the effects of carbon dioxide in shielding gas on arc plasma and metal droplet formation. However, in their model, the weld pool dynamics was neglected and the workpiece was treated as a flat plate and the effects of shielding gas on bead shape and penetration depth were omitted. Jönsson *et al.*[24] numerically investigated the argon arc and helium arc in GMAW at a variety of current levels and also discussed the metal transfer behaviors using their predicted arc parameters. However, their model cannot directly predict the metal transfer, and the electrode tip and weld pool surface were also assumed to be flat. In reality, the profile of the electrode tip changes rapidly, and the weld pool surface is highly deformable. When the droplet transfers through arc plasma, the flow of arc plasma is dramatically distorted and, hence, the distributions of temperature, velocity, and current in plasma arc significantly vary during the welding.

In this work, a comprehensive model is employed to simulate the time-dependent, coupled transport phenomena occurring during the GMAW process in different shielding atmospheres. The effects of shielding gas compositions, including pure argon and argon-helium mixtures with various molar percentages of argon (75% Ar, 50% Ar, and 25% Ar), are studied in terms of (1) the characteristics of plasma arc and (2) the droplet formation, detachment, transfer, and impingement onto the weld pool, and weld pool dynamics and weld bead profiles. This work provides a better understanding of the fundamental physics involved on the effects of shielding gas compositions and the essential knowledge that may help the selection of shielding gas to achieve better weld quality in GMAW.

II. MATHEMATICAL MODEL

The model developed by Hu and Tsai[20,21] is modified and used in the present study. The governing differential equations and the numerical technique are the same as before and, here, only the main features of the model are outlined below.

Figure 1 is a schematic sketch of a stationary axisymmetric GMAW system. In this system, a constant current is supplied to the electrode (anode) that is continuously fed downward through the contact tube at the top of the system. A plasma arc is struck between the electrode and the workpiece (cathode). The electrode is melted at its tip by high temperature arc, and droplets are formed and then detached and transfer to the workpiece. A weld pool is formed at the workpiece by the continuous impingement of the droplets and the dynamic interaction with the arc plasma. Inert shielding gas is provided through the shielding gas nozzle. In this model, only half of the entire physical domain, ABCDEFGA, Fig. 1, is considered due to symmetry along the centerline AG. The calculation domain is divided into two regions: the arc region and the metal region. The metal region includes the electrode, the workpiece, and the droplet. The arc region and metal region are calculated separately and coupled

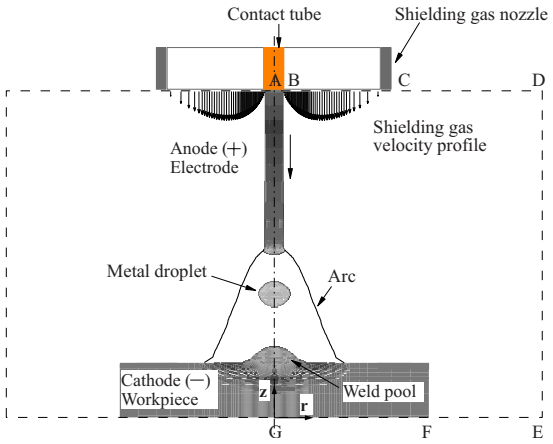

FIG. 1. (Color online) A schematic representation of a GMAW system (not to scale).

through the special boundary conditions at the metal-plasma interfaces.[25,26] In this model, the time-dependent conservation equations for mass, momentum, and energy together with current continuity, Ohm's law, and Maxwell's equations in cylindrical r-z coordinate system are used to determine the basic physical parameters describing the transport phenomena in arc plasma and metal, including the pressure p, radial and axial velocities v_r and v_z, temperature T, electrical potential ϕ, radial and axial current densities J_r and J_z, and self-induced azimuthal magnetic field B_θ. The input material properties for arc plasma and metal include density ρ, viscosity μ, specific heat c, thermal conductivity k, electrical conductivity σ_e, permeability function K, enthalpy h, and inertial coefficient C.

A fixed computational domain is used to solve the equations in the arc region. Note that the effect of metal vapor on plasma properties is omitted in the present study. The plasma is assumed to be in laminar flow, local thermodynamic equilibrium[26] (LTE) and optically thin; thus the radiation may be modeled in an approximate manner by defining a radiation heat loss per unit volume. The metal region is used as the inner boundary for the arc region. As the velocity in the metal domain is much smaller than the velocity of arc plasma, the metal region serves as an inner obstacle in the arc domain. The temperature at the metal free surface is considered as the temperature boundary for the arc domain. At the plasma-electrode interface, there exist anode and cathode sheath regions.[26] In these regions, the mixture of plasma and metal vapor departs from LTE; thus it no longer complies with the general energy equation. Since the sheath region is very thin [about 0.02 mm (Ref. 26)], it is treated as a special interface to take into account the thermal effects on the plasma. At the arc-anode/cathode interface, the cooling effects through conduction are included in the energy equation for the plasma as the source terms.[20]

For the metal, the enthalpy is used to describe the energy equation; thus the solid/liquid phase-change boundaries are handled by the continuum model[27] that tracks different phases using the solid mass fraction f_s and liquid mass fraction f_l. The liquid region ($f_l=1$), mushy zone ($0<f_l<1$, $0<f_s<1$), and solid region ($f_s=1$) are all calculated by the same momentum equations. In the mushy zone, the

latent heat is absorbed or released during the fusion and solidification processes. Within the computational domain, the moving surface of the electrode, droplet, and weld pool forms the inner boundary for the arc region. The VOF equation is solved in the metal domain to track the moving free surface as free boundary conditions for the metal domain. When averaged over the cells of a computing mesh, the average value of VOF function F in a cell is equal to the fractional volume of the cell occupied by the metal. The molten part of the metal is subjected to body forces such as gravity and electromagnetic force. It is also subjected to surface forces such as surface tension due to surface curvature, Marangoni shear stress due to temperature difference, arc plasma shear stress, and arc pressure at the arc plasma and metal interface. The arc pressure at the metal surface is obtained from the computational result in the arc region. Using the VOF function as the characteristic function, these surface forces are all transformed to the localized body forces and added to the momentum transport equations as source terms at the boundary cells according to the continuum surface force (CSF) model. The detailed mathematical formulation for each surface force is given in Ref. 20, and the use of VOF function to handle the surface cells can be found in Ref. 28. The method to convert the surface force to the localized body force via the CSF model is available in Refs. 29 and 30. At the plasma-electrode interface, additional source terms are added to the energy equation for the special treatment of the anode sheath and the cathode sheath. The additional thermal sources to the anode include thermal conduction from the plasma to the anode, the electron heating associated with the work function of the anode material, the black body radiation loss from the anode surface, and the heat loss due to the evaporation of electrode materials. Since the thermal effect due to the cathode sheath has been omitted in many models and reasonable results were obtained,[13–17] only the conduction, radiation, and evaporation terms are considered in the energy balance equation at the cathode surface.

In the present study, the transport phenomena in the metal and the arc plasma are calculated separately in the corresponding metal domain and arc domain, and the two domains are coupled through the interfacial boundary conditions at each time step. The current continuity equation and its associated boundary conditions are solved for the entire domain, while other primary variables, including p, u, v, and T, are separately calculated in the metal domain and arc domain in an iterative manner. Iterations are required to assure convergence of each domain and then the boundary conditions are calculated from each domain for the coupling between the two domains. For the metal domain, the method developed by Torrey *et al.*[28] was used to solve p, u, v, and T. This method is Eulerian and allows for an arbitrary number of segments of free surface with any reasonable shape. For the arc domain, a fully implicit formulation is used for the time-dependent terms, and the combined convection/diffusion coefficients are evaluated using an upwind scheme. The SIMPLE algorithm[31] is applied to solve the momentum and mass continuity equations to obtain the velocity field in the plasma arc.

The calculation domain is half of the cylinder of 5.0 cm in radius and 3.05 cm in length. Extensive tests using different grid sizes and time step sizes have been conducted to assure consistent results. The final grid and time step sizes used in the present study can be considered as the compromised values between computational time and accuracy. A nonuniform grid point system is employed with finer grid sizes near both the cathode and the anode. The mesh sizes near the anode and cathode center are set as 0.01 cm. The time step size is set as 5×10^{-6} s.

III. RESULTS AND DISCUSSION

In this section, the basic physical parameters in the arc and in the metal for pure argon and argon-helium mixtures with various molar argon contents (75% Ar, 50% Ar, and 25% Ar) are presented. Generally, welding conditions employed for various shielding gases are quite different, including the current, arc length, wire feed speed, gas flow rate, and so on.[1] However, the intent of this study is to compare the effects of shielding gas compositions in GMAW and, hence, for comparison purpose, these welding conditions are assumed to be the same for various shielding gases. The constant current is set at $I=240$ A. A 1.6-mm-diameter wire of mild steel is fed continuously toward the workpiece at a wire feed speed of 5.0 cm/s. The workpiece is also a mild steel disk with a 3 cm diameter and a 0.5 cm thickness. The imposed external shielding gas flows out of a 1.91 cm gas nozzle at a rate of 24 l/min. The contact tube is set flush with the bottom of the gas nozzle and is 2.55 cm above the workpiece. The initial arc length is set as 0.8 cm. Note that the aforementioned values of welding parameters are typical in a GMAW process.[1] The thermophysical properties of mild steel and the other parameters used in the calculation are summarized in Table I. Temperature-dependent physical properties of pure Ar,[32,33] pure He and Ar–He mixtures at equilibrium,[33–35] and volume radiation heat loss (S_R) (Ref. 32) are drawn in Fig. 2. Due to the lack of radiation coefficients for pure He and Ar–He mixtures, the data of Ar (Ref. 32) are used for all cases, which does not lead to unreasonable results.[24]

In practice, a touch striking or a pilot starting arc is needed to initiate the main electric arc for welding. In this study, an initial high temperature ($T=25\,000$ K) arc column is assumed for arc initiation, which can be sustained by itself and reaches the working status after several numerical iterations for all cases. The time is set as $t=0$ s when the arc is established. However, the calculation for pure helium was diverged because the electrical conductivity for pure helium is so small at temperature up to 9000 K (as shown in Fig. 2) that an arc cannot be sustained by itself. Also, in practice, pure helium has seldom been used as shielding gas because of the arc instability. Hence, we do not consider pure helium in this study.

In order to better explain the transport phenomena, the selected instants for each subfigure are different, and the time intervals between two subfigures are not equal either. In order to increase the readability of vectors, only a quarter of the grid nodes are used for plotting the distributions of ve-

TABLE I. Thermophysical properties of mild steel and other parameters.

Nomenclature	Symbol	Value (unit)
Specific heat of solid phase	c_s	700 (J kg^{-1} K^{-1})
Specific heat of liquid phase	c_l	780 (J kg^{-1} K^{-1})
Thermal conductivity of solid phase	k_s	22 (W m^{-1} K^{-1})
Thermal conductivity of liquid phase	k_l	22 (W m^{-1} K^{-1})
Density of solid phase	ρ_s	7200 (kg m^{-3})
Density of liquid phase	ρ_l	7200 (kg m^{-3})
Thermal expansion coefficient	β_T	4.95×10^{-5} (K^{-1})
Radiation emissivity	ε	0.4
Dynamic viscosity	μ_l	0.006 (kg m^{-1} s^{-1})
Latent heat of fusion	H	2.47×10^{5} (J kg^{-1})
Latent heat of vaporization	H_{ev}	7.34×10^{6} (J kg^{-1})
Solidus temperature	T_s	1750 (K)
Liquidus temperature	T_l	1800 (K)
Ambient temperature	T_∞	300 (K)
Vaporization temperature	T_{ev}	3080 (K)
Surface tension coefficient	γ	1.2 (N m^{-1})
Surface tension temperature gradient	$\delta\gamma/\delta T$	10^{-4} (N m^{-1} K^{-1})
Work function	ϕ_w	4.3 V
Electrical conductivity	σ_e	7.7×10^{5} (Ω^{-1} m^{-1})
Shielding gas flow rate	Q	24 (l min^{-1})
Internal diameter of shielding gas nozzle	R_n	19.1 (mm)
Welding current	I	240 (A)
Electrode diameter	d	1.6 (mm)
Wire feed speed	V_w	5 (cm s^{-1})

locity, current, and electromagnetic force in the arc, and a half of the grid nodes are used for those in the metal. Note that the shapes of the electrode and workpiece in all figures are marked with thick solid lines. Tremendous amount of results have been obtained in the calculation; however, in the following, only some selected results will be presented. The transport phenomena of plasma arc will be discussed first, and then followed by the results of metal transfer. As the plasma arc and metal transfer are coupled together, cross-reference discussions between them are necessary in order to well explain the very complex transport phenomena.

A. Arc plasma

Figure 3 shows the temperature distributions and the sequence of droplet generation and the associated arc plasma for different shielding gases. Before the droplet is detached from the electrode tip, the first and second columns of Fig. 3, a high temperature arc cone is formed underneath the droplet and it expands outward and downward for each case, resulting in the decrease in its temperature toward the workpiece surface. The maximum temperature occurs on the axis near the bottom of the droplet, which are, respectively, 21 620, 21 680, 22 290, and 21 850 K for pure Ar, 75% Ar, 50% Ar, and 25% Ar at $t=50$ ms. Because of the high thermal conductivity for helium at about $T>15\,000$ K (shown in Fig. 2), the addition of helium to argon helps produce a larger hot core in the upper part of the arc column. The addition of helium to argon results in a higher arc voltage that is required to maintain the arc stability between the anode and the cathode. For example, at $t=50$ ms as shown in Fig. 4, the electrical potential contours are higher as helium content increases, and the arc voltages are, respectively, 15.72, 17.37, 19.66, and 23.52 V for pure Ar, 75% Ar, 50% Ar, and 25% Ar. This is caused by the higher ionization potential and hence the lower electrical conductivity (see Fig. 2) at a higher helium content. The higher arc voltage increases the energy input at a constant current and, hence, contributes to the aforementioned increase in arc temperatures for higher helium contents. However, because the lower part of the arc column is at lower temperatures, there is a sharp decrease in the degree of ionization for the mixture with a large amount of helium addition (e.g., 25% Ar). Due to less ionization, the temperature in the lower part decreases, leading to a slightly decrease in the length of the hot arc column for 25% Ar. As the plasma temperature is mainly caused by Joule heating, the temperature distribution of the plasma arc, shown in Fig. 3, is proportional to the magnitude and distribution of the current.

As shown in Fig. 5, the current generally diverges from the electrode tip, converges at the cathode (workpiece), and then diverges in the workpiece for all cases. Before droplet detachment, the first and second columns of Fig. 5, the current converges to the surface of the workpiece at a continuous area (i.e., a "disk" shape) for pure Ar, 75% Ar, and 50% Ar, while for 25% Ar, the current converges to a "ring" or "circle" (from an axisymmetric standpoint) around the center of the workpiece. The phenomena of current convergence can be more clearly seen in Fig. 6(a) which shows the distributions of current density along the workpiece surface. For argon-rich cases (pure Ar and 75% Ar) the current density distribution is fairly smooth and uniform near the center $r=0$ with its peak at the center. For 25% Ar, there are two peaks at the arc fringe (which actually is a ring or circle because of an axisymmetric coordinate); the current density near the center is quite low (like a "valley"), and the peaks coincide with the ring of the converged current, as shown in Fig. 5(d), and the ring of high temperatures in Fig. 3(d). For 50% Ar, the current density distribution along the workpiece has the characteristics that are a combination of the results for argon rich and helium rich as discussed above. It is seen that a small disk with continuous high current density appears near the center, but the current density at the arc fringe fluctuates significantly with two peaks occurring. For all cases, the current density decreases abruptly near the arc fringe and thereafter becomes negligible. From Figs. 5 and 6, it is interesting to find that the high helium content results in a significant arc contraction near the electrode tip and the workpiece surface as compared to pure Ar. This is primarily because of the high ionization potential of helium, which leads to a sharper decrease in electric conductivity at lower arc temperatures as the helium content increases. The arc contraction has significant effects on the droplet generation, metal transfer, and weld penetration in the workpiece, which will be discussed below.

It should be noted that current convergence at the cathode (workpiece) is related to electron emission at the cathode, and the physics involved are extremely complex and not well understood.[13–17] Hence, the results discussed above on current convergence and the associated current density distribution at the cathode are mainly due to plasma effects and

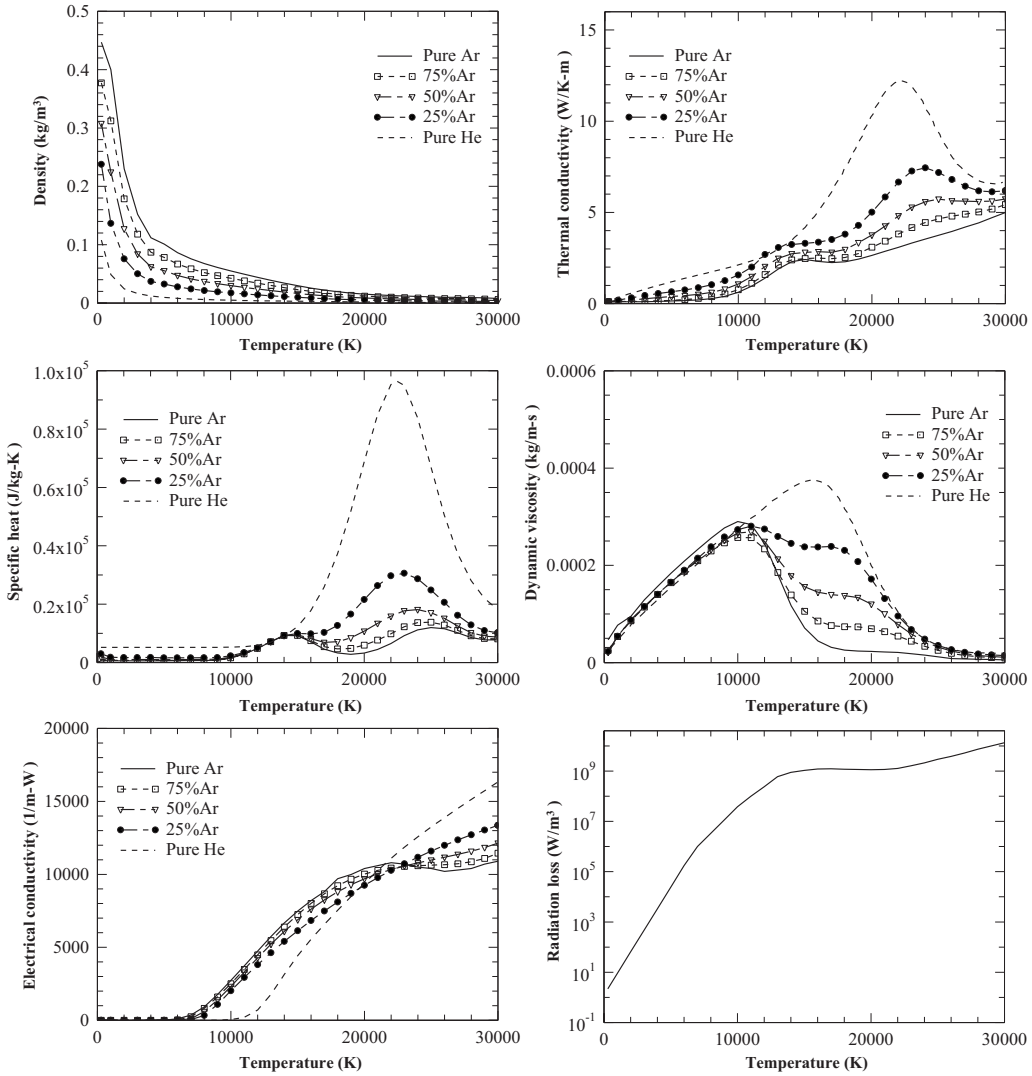

FIG. 2. Temperature-dependent material properties of shielding gases and the volume radiation heat loss taken from Refs. 32–35.

are not impacted by the cathode ability to emit the arc current. The model to handle the anode sheath and cathode sheath including electron emission can be found in Ref. 36.

The aforementioned current flow pattern shown in Fig. 5 determines the direction of the electromagnetic force in the arc and the metal. As shown in the first and second columns of Fig. 7, the electromagnetic force in the arc underneath the electrode tip is radially inward and axially downward and is inward and upward near the workpiece for all cases. Due to the action of the electromagnetic force, therefore, the plasma is accelerated and flows inward and downward with very high velocities. The downward arc plasma reaches the workpiece and, thereafter, flows outward due to the stagnation effect (as shown in the first and second columns of Fig. 8). The arc plasma has very high velocities which increase with the helium content. For example, the maximum downward velocities at $t=50$ ms are, respectively, about 320, 335, 410, and 450 m/s for pure Ar, 75% Ar, 50% Ar, and 25% Ar. With the increase in helium content, the arc contraction and the current convergence near the workpiece increase. As a result, stronger inward and upward electromagnetic forces and the resulting arc flows are found near the workpiece for helium-rich gases, which counteract the downward and outward flows from the electrode. However, these opposite inward and upward flows caused by the local electromagnetic force near the workpiece are weaker and cannot overcome the stronger downward and outward flows from the electrode. This conclusion may not be true, especially at $t=280$ ms for 25% Ar, which will be discussed next.

As shown in the third and fourth columns of Fig. 3, after the droplet is detached from the electrode, a new arc column is formed between the electrode tip and the top of the detached droplet. Due to the lower ionization potential of argon, it is easier for argon-rich cases to re-establish a new arc. Hence, for argon-rich cases, higher arc temperatures above the top of the droplet are observed when the droplet has just been detached, the third column of Fig. 3. On the other hand, just after detachment, the temperature underneath the droplet is still relatively high in argon-rich cases, and thus the current can flow through the detached droplet, as shown in the third column of Fig. 5. In contrast, as the helium content increases, less current flows through the detached droplet; especially for 25% Ar, there are almost no current flows through the detached droplet. The detached droplet blocks the arc plasma flows downward resulting in lower temperatures below the detached droplet, the third column of Fig. 3,

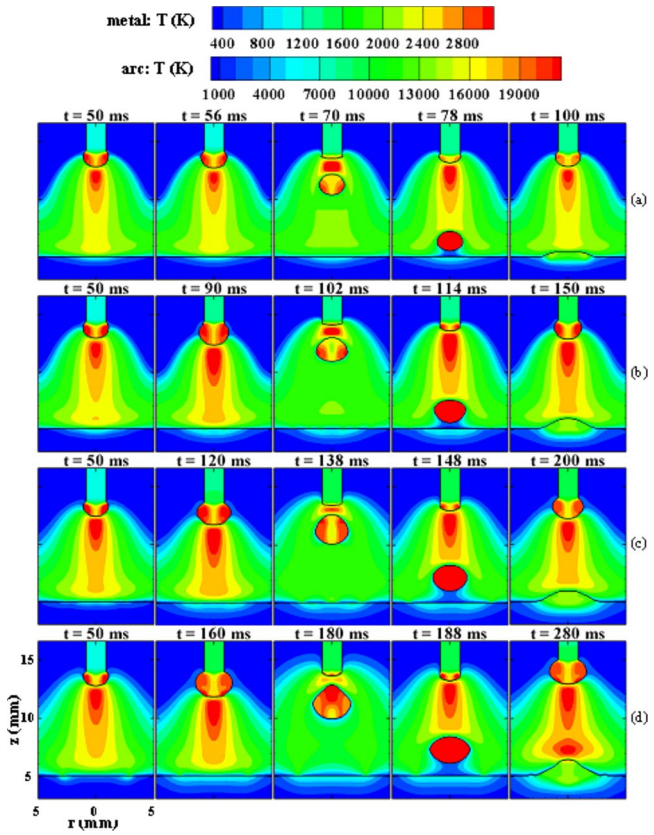

FIG. 3. (Color online) The sequence of temperature distribution in the arc and the metal for different shielding gases, showing the typical processes of arc formation and evolutions, droplet formation, detachment, transfer, and impingement onto the workpiece: (a) pure Ar, (b) 75% Ar, (c) 50% Ar, and (d) 25% Ar.

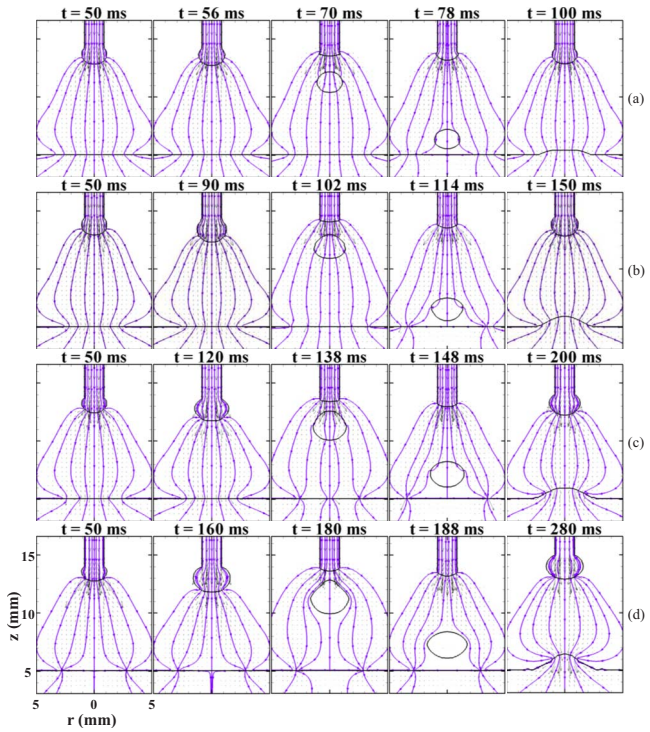

FIG. 5. (Color online) The corresponding current distribution in the arc and the metal for the cases shown in Fig. 3: (a) pure Ar, (b) 75% Ar, (c) 50% Ar, and (d) 25% Ar.

and plasma arc expansion, the third column of Fig. 8, for all cases. When the droplet further moves downward, the fourth column of Fig. 3, the new arcs expand and are "stretched" between the electrode tip and the falling droplet. While the arc temperature underneath the droplet continues to decrease, more current flows bypass around the falling droplet in all cases, the fourth column of Fig. 5. After bypassing the detached droplet, the current flows converge to an annular area (for argon-rich cases) or a ring or circle (for high helium content) at the workpiece surface, as shown in the fourth column of Fig. 5, rather than a continuous area (disk) shown in the first column of Fig. 5.

As shown in the fifth column of Fig. 3, after the first droplet impinges onto the workpiece, a new arc exists between the electrode and the workpiece for all cases, similar to the phenomena before detachment, as shown in the first column. For 25% Ar, however, the distance between the electrode tip and the workpiece is shorter, which results in "double hot spots:" one is beneath the electrode and the other is above the workpiece at $t=280$ ms in Fig. 3(d). The plasma

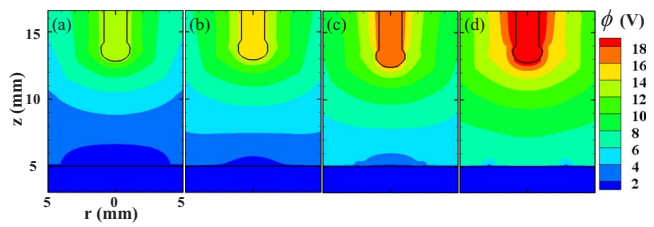

FIG. 4. (Color online) The electrical potential distribution at $t=50$ ms: (a) pure Ar, (b) 75% Ar, (c) 50% Ar, and (d) 25% Ar.

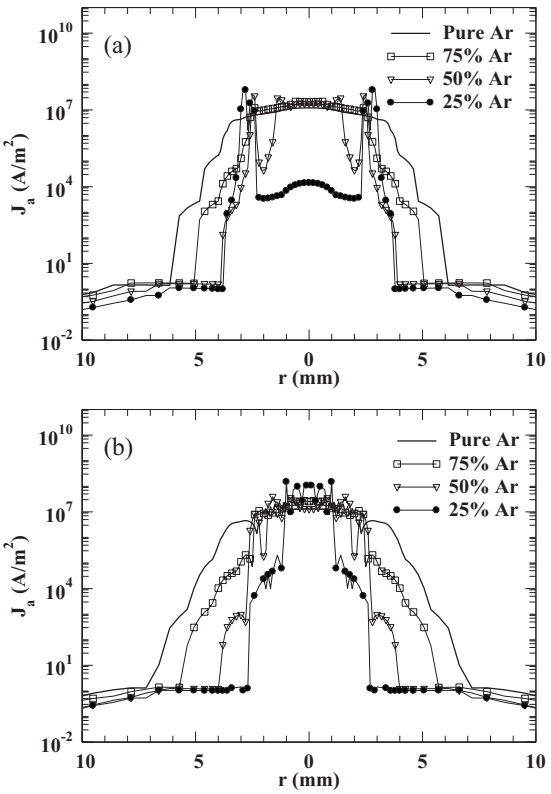

FIG. 6. The current density distributions along the workpiece surface at different instants corresponding to the cases shown in Fig. 5: (a) the first column and (b) the fifth column.

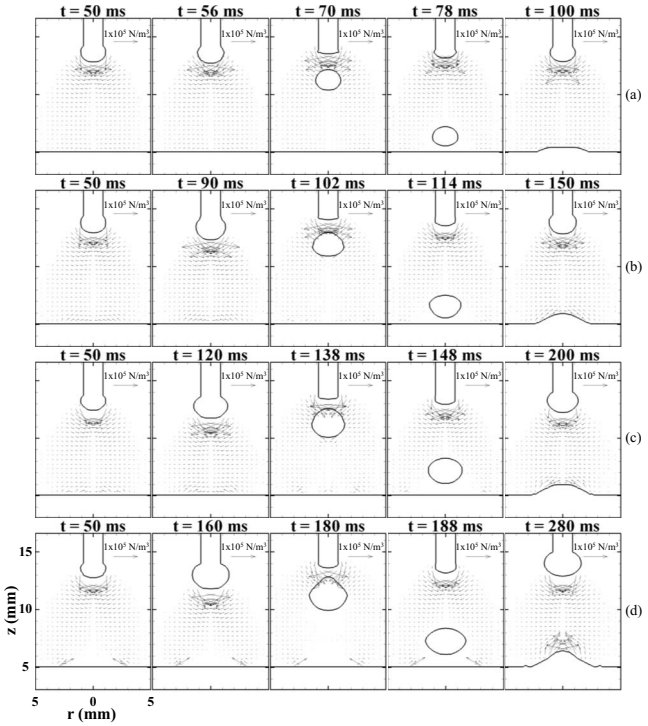

FIG. 7. The corresponding electromagnetic force distribution in the arc for the cases shown in Fig. 3: (a) pure Ar, (b) 75% Ar, (c) 50% Ar, and (d) 25% Ar.

arc column looks like it is being "squeezed" and "bulged." The lower hot spot is caused by the strong current convergence and, hence, the intensive Joule heating, Fig. 5(d). For all cases, after the droplet impingement, the current flows

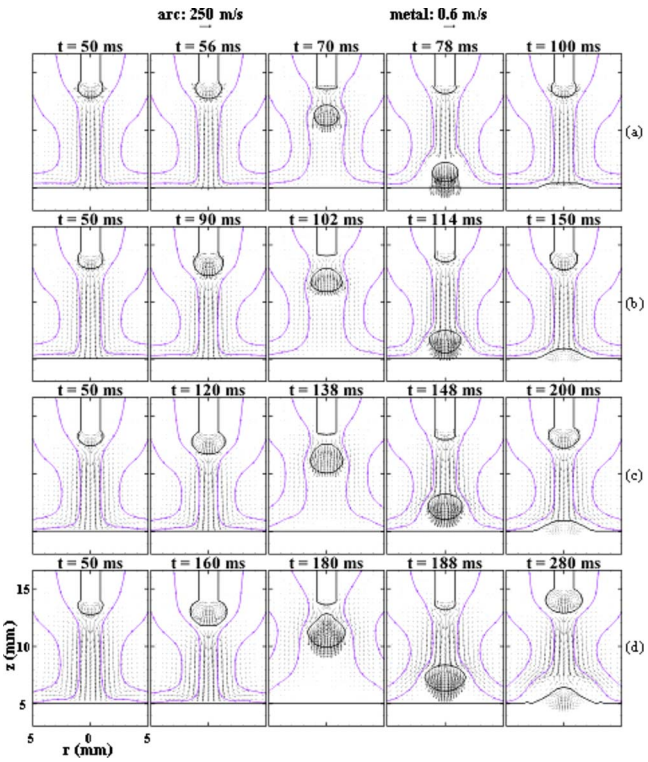

FIG. 8. (Color online) The corresponding velocity distribution in the arc and the metal for the cases shown in Fig. 3: (a) pure Ar, (b) 75% Ar, (c) 50% Ar, and (d) 25% Ar.

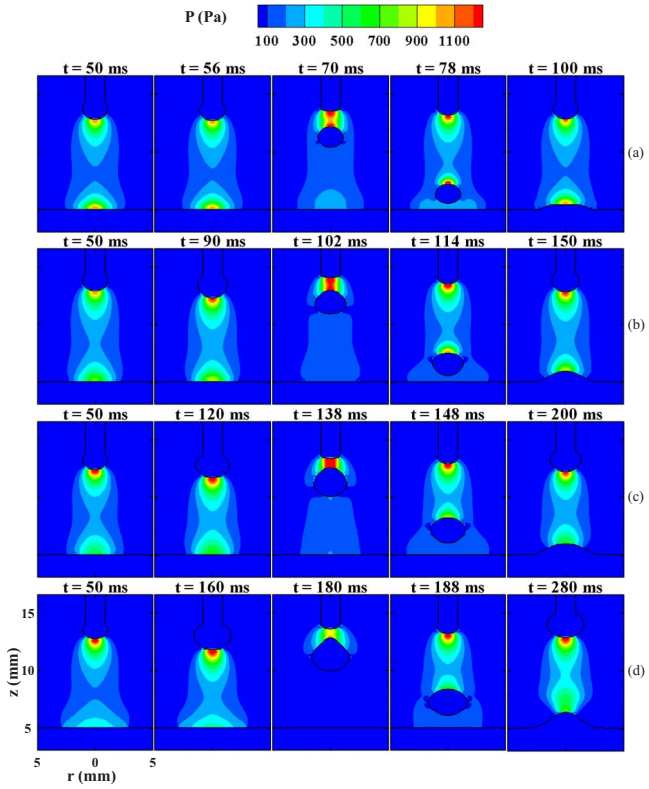

FIG. 9. (Color online) The corresponding arc pressure distribution for the cases shown in Fig. 3: (a) pure Ar, (b) 75% Ar, (c) 50% Ar, and (d) 25% Ar.

converge at continuous areas (disks) of the workpiece. The convergence area decreases as the helium content increases, which can also be seen in Fig. 6(b), showing that the scope of high current density along the workpiece decreases with the increase in helium content. This causes a significant arc contraction, Fig. 5. The current density distribution along the workpiece shows a "zigzag" fluctuation in the vicinity of the center, Fig. 6(b). For 25% Ar, the very severe arc contraction induces a strong upward electromagnetic force near the weld pool, as shown at $t=280$ ms in Fig. 7(d), which, therefore, creates vortices near the weld pool surface at $t=280$ ms in Fig. 8(d).

Figure 9 shows the corresponding arc pressure contours in the arc. It is seen in the first and second columns that there are two high pressure regions before the droplet detachment. One is underneath the electrode, and the other is near the workpiece. The high pressure underneath the electrode is caused by the pinch effect of the electromagnetic force, Fig. 8, and the high pressure near the workpiece is because of the stagnation of the plasma flow. With the increase in helium in the mixture, the inward and upward arc flows counteract the downward and outward flows from the electrode, as discussed before, which decreases the arc pressure near the workpiece for higher helium mixtures. After the droplet is detached, the third and fourth columns in Fig. 9, new high pressure regions exist between the electrode tip and the upper surface of the falling droplet. After the droplet impinges onto the workpiece, the arc pressure distribution resumes to the two high pressure regions similar to the first and second

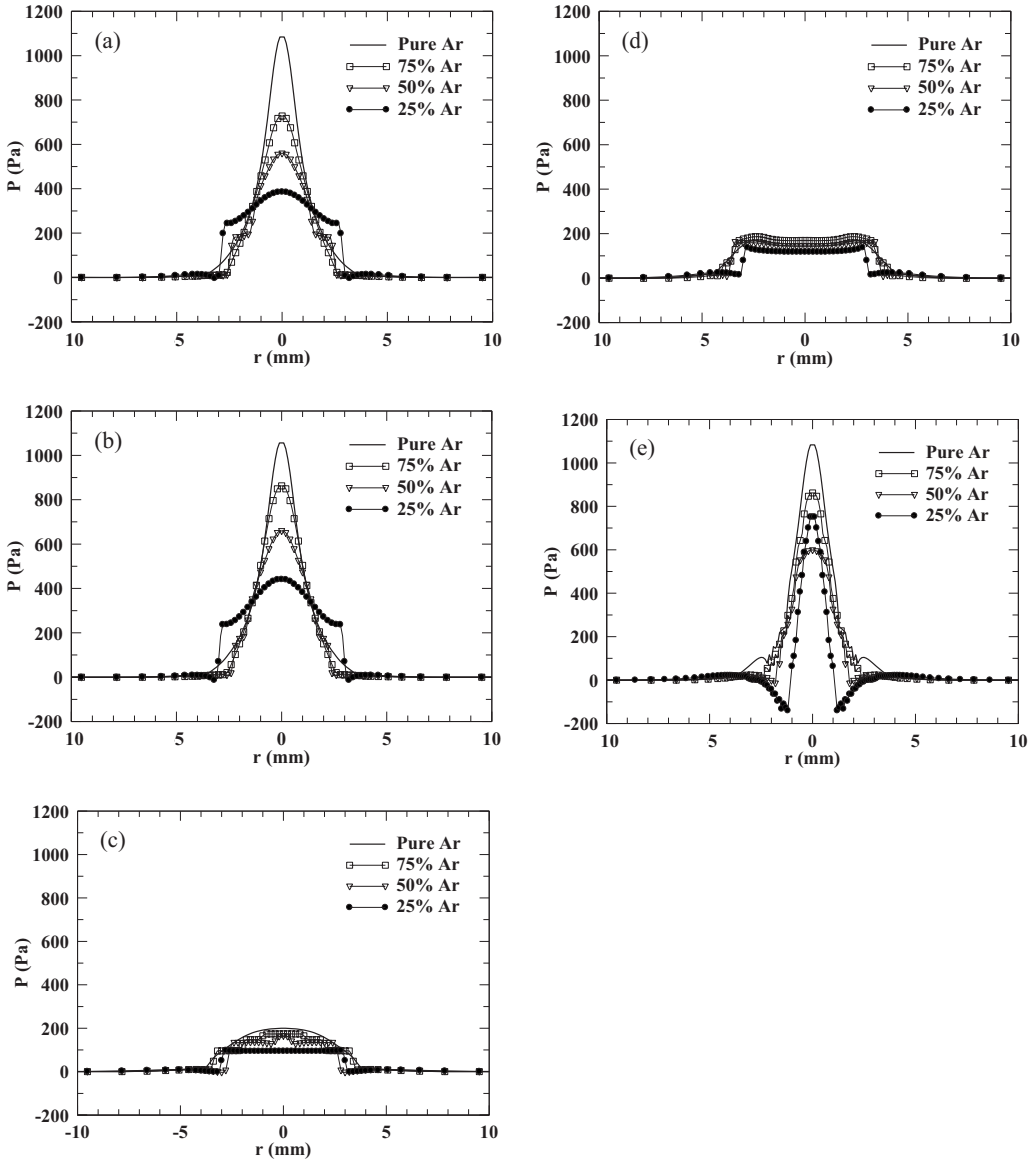

FIG. 10. The arc pressure distributions along the workpiece surface at different instants corresponding to the cases shown in Fig. 9: (a) the first column, (b) the second column, (c) the third column, (d) the fourth column, and (e) the fifth column.

columns, except for the case of 25% Ar, in which the two high pressure regimes join each other, similar to the temperature shown in Fig. 3(d).

To further clarify the changes in arc pressure, Fig. 10 shows the magnitudes of arc pressure along the workpiece surface corresponding to the cases in Fig. 9. Before the droplet detachment, Figs. 10(a) and 10(b), the arc pressure generally has a Gaussian-like distribution that decreases to nearly zero at about $r=3$ mm, except for the case of 25% Ar, in which the pressure is more uniform near the center and abruptly decreases to a minimum of -10 Pa below the ambient pressure just outside the arc fringe. The peak of the arc pressure obviously decreases as the helium content increases. When the detached droplet is in between the electrode and the workpiece, the third and fourth columns in Fig. 3, the plasma arc is blocked by the droplet, and the arc pressures along the workpiece surface are rather uniform but very small, and they do not differ very much for all cases, as shown in Figs. 10(c) and 10(d). The scope of high pressure range does not differ significantly between different helium contents, except for the case when the droplet impinges onto the workpiece, Fig. 10(e), in which the scope of the high pressure is significantly smaller for all cases, and the scope decreases as the helium content increases. A negative pressure as low as -140 Pa below the ambient pressure is predicted after the droplet impinges onto the workpiece, Fig. 10(e) for 25% Ar.

B. Metal transfer

The solid electrode is melted by the surrounding high temperature arc and generates a droplet at the tip. The droplet continues to grow until it is detached from the electrode. As shown in Fig. 3, the droplets are, respectively, detached at about $t=68$, 100, 135, and 176 ms for pure Ar, 75% Ar, 50% Ar, and 25% Ar. For all cases, the droplet sizes are larger than the electrode diameter; thus, the metal transfer is in the globular regime. As seen in Fig. 3, it takes a longer time to

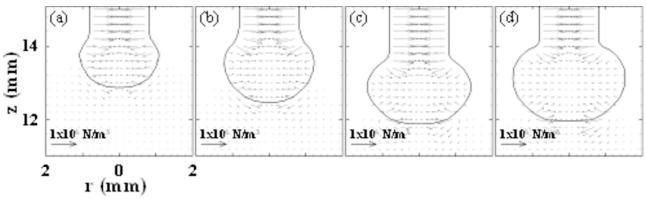

FIG. 11. (Color online) The distributions of electromagnetic forces acting on the droplets for (a) pure Ar (t=56 ms), (b) 75% Ar (t=90 ms), (c) 50% Ar (t=120 ms), and (d) 25% Ar (t=160 ms).

form a droplet and the droplet size increases as the helium content increases. The predicted results are consistent with the experimental observation[8] that the droplet frequency using argon is much higher than that for helium at the same current input. The droplet detachment is determined by the competition of several forces acting on the droplet, including the arc pressure, surface tension, gravity, plasma shear stress, and electromagnetic force. Arc pressure underneath the droplet and the surface tension are attaching forces that tend to uphold the droplet at the electrode tip. The gravity and plasma shear stress are detaching forces that tend to separate the droplet from the electrode tip. As discussed above, the increase in helium content corresponds to a higher pressure in the arc underneath the droplet. For example, at the second column of Fig. 9, the maximum arc pressures underneath the droplet are, respectively, 1083, 1227, 1297, and 1344 Pa above the ambient pressure for pure Ar, 75% Ar, 50% Ar, and 25% Ar. The high arc pressure contributes to the increase in droplet formation time in helium-rich gases. The electromagnetic force, which is affected by the shielding gas composition, has a profound effect on droplet generation which is discussed below.

As shown in Fig. 5, the current flows in the electrode are mostly parallel to the axis, which slightly diverge along the top of the droplet and flow out of the electrode from the lower part of the droplet. Therefore, for all cases, the radial component of the electromagnetic force in the electrode is inward, as shown in the enlarged Fig. 11, and has a pinch effect on the droplet and thus it is a detaching force. For pure Ar, the axial component of the electromagnetic force is downward and is a detaching force that pushes the liquid metal downward. With the increasing helium content, however, the arc contraction underneath the droplet causes more current flows leaving the droplet from a small area of the bottom surface, which increases the current density and produces an upward electromagnetic force for repelling the droplet, as shown in Fig. 11. Therefore, when helium is added to the shielding gas, the axial component of the electromagnetic force in the upper part of the droplet is still a detaching downward force, while at the bottom, the axial electromagnetic force is an attaching upward force that sustains the droplet. Especially for 25% Ar, at t=160 ms in Fig. 8(d), the melt-flow at the bottom of the droplet is upward, which is caused by the significant upward electromagnetic force, Fig. 11(d). As a result of the aforementioned two opposite forces acting on the droplet, the droplet is squeezed to become an oblate shape, and the longer droplet formation time is required as the helium content increases.

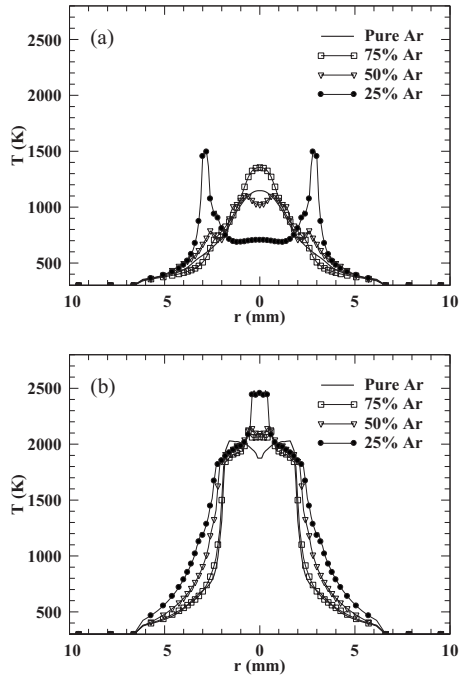

FIG. 12. The metal temperature along the workpiece surface at different instants corresponding to the cases shown in Fig. 3: (a) the first column and (b) the fifth column.

After the droplet is detached from the electrode, at the balance of various forces acting on the droplet, including the electromagnetic force, gravity, arc pressure, and plasma shear stress, the droplet is accelerated to the workpiece. These forces also change the shape of the droplet during its flight in the arc. When the falling droplet is in between the electrode and the workpiece, it continues to be heated by the surrounding high temperature plasma arc. However, as shown in the fourth column of Fig. 3, before the droplet impinges onto the workpiece, the temperature distribution in the droplet becomes more uniform which is caused by the mixing vortices, Fig. 8, between the hot fluid along the surface of the droplet and cold fluid near the center. The droplet hits the workpiece surface with a rather high axial velocity. At the instants just right before the droplet impinges onto the workpiece, the axial velocities of the droplet are, respectively, 56.8, 54.2, 52.3, and 52.0 cm/s for pure Ar, 75% Ar, 50% Ar, and 25% Ar, the fourth column of Fig. 8.

Figure 12 shows the metal temperature along the workpiece surface at different instants corresponding to the first and fifth columns in Fig. 3. The temperature increase in the workpiece is the combined result of Joule heating, heat flux from arc plasma, and thermal energy carried by droplet. At t=50 ms, Fig. 12(a), the temperature profile for argon-rich cases is a standard Gaussian-like distribution. However, for 75% Ar, the workpiece surface temperatures near the center are higher than those for pure Ar, which is caused by the current convergence to a smaller area for 75% Ar, as indicated in Fig. 6(a). For 50% Ar and 25% Ar, the temperature distributes like an M-shape with two peaks (the peak temperatures form a ring or circle shape in an axisymmetric

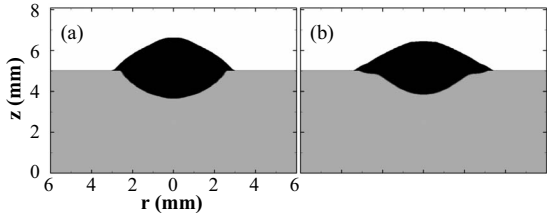

FIG. 13. The solidified weld bead and penetration profiles for different shielding gases: (a) pure Ar and (b) 25% Ar.

coordinate system) at which the current converges, as shown in Fig. 6(a). The aforementioned valley current for 25% Ar in Fig. 6(a) causes a rather low temperature at the center in Fig. 12(a). After the droplet impinges onto the workpiece, the workpiece is melted, and a weld pool is formed, the fifth column of Fig. 3, the workpiece surface temperature increases significantly, Fig. 12(b). As shown in Fig. 12(b), the temperature profiles along the surface of the workpiece for all cases are very similar in shape and smooth except near the center of the workpiece at which the temperatures fluctuate. At the same location, however, the temperature increases as the helium content increases because of larger droplet size. Note that the temperature profile for different helium contents is at different instants.

The mass, momentum, and thermal energy carried by droplets are merged into and mix with the workpiece. The current is turned off at $t=0.4$ s and then solidification begins. At this instant, the numbers of droplets impinge onto the workpieces are, respectively, 5 and 2 for pure Ar and 25% Ar. The solidified weld bead profile, characterized by the bead width, bead height, and penetration depth, is one of the important parameters for assessing weld quality. The typical bead profile is divided into two areas/volumes: one is the area of the base material that was melted and the other is the area of metal above the original workpiece surface and is called reinforcement. Figure 13 shows the weld bead profile for the cases of pure Ar and 25% Ar. It is seen that the weld bead with pure argon has a greater penetration, while a wider bead is found for 25% Ar.

IV. CONCLUSIONS

A comprehensive model has been employed to study the influences of shielding gas compositions on arc plasma and metal transfer in GMAW. The transient transport phenomena in the plasma arc and the metal for the GMAW process shielded by pure Ar, 75% Ar+25% He, 50% Ar +50% He, and 25% Ar+75% He at a constant current were presented. From the results of this study, it is found that the shielding gas compositions have pronounced effects on arc characteristics, droplet formation, metal transfer, and weld bead profile.

It is easier for Ar to establish a plasma arc due to lower ionization potential as compared to helium. The addition of helium helps produce a larger hot arc core because of the higher thermal conductivity, but the further increase in helium may decrease the degree of ionization. For high helium content, the arc contraction appears near the electrode and the workpiece. As a result, a significant upward electromagnetic force is formed near the workpiece which leads to the distorted distribution of arc parameters. Arc contraction also has significant effects on droplet formation and detachment. In pure Ar shielding, the axial component of the electromagnetic force acting on the droplet is a detaching force that contributes to the separation of the droplet from the electrode. As the helium content increases, the axial electromagnetic force at the bottom of the droplet becomes an attaching force and the arc pressure underneath the droplet significantly increases due to arc contraction which sustains the droplet at the electrode tip and squeezes the droplet to become an oblate. Therefore, the increase in helium content corresponds to the larger droplet size and less droplet detachment frequency for welding at a constant current. For higher helium content in the shielding gas, a wider weld bead but shallower penetration depth is predicted.

[1]R. L. O'Brien, *Welding Handbook*, 8th ed. (American Welding Society, Miami, FL, 1991), Vol. 2.
[2]N. Stenbacka and K. A. Persson, Weld. J. (Miami, FL, U.S.) **68**, 41s (1989).
[3]M. Ushio, K. Ikeuchi, M. Tanaka, and T. Seto, Weld. Int. **9**, 462 (1995).
[4]W. D. A. Macedo and R. D. C. Torres, U.S. Patent No. 6,111,219 (29 August 2000).
[5]J. M. Kuk, K. C. Jang, D. G. Lee, and I. S. Kim, J. Mater. Process. Technol. **155–156**, 1408 (2004).
[6]I. Pires, L. Quintino, and R. M. Miranda, Mater. Des. **28**, 1623 (2007).
[7]E. J. Soderstrom and P. F. Mendez, Weld. J. (Miami, FL, U.S.) **87**, 124s (2008).
[8]S. Rhee and E. Kannatey-Asibu, Weld. J. (Miami, FL, U.S.) **71**, 381s (1992).
[9]L. A. Jones, T. W. Eagar, and J. H. Lang, Weld. J. (Miami, FL, U.S.) **77**, 135s (1998).
[10]Q. Lin, X. Li, and S. W. Simpson, J. Phys. D: Appl. Phys. **34**, 347 (2001).
[11]L. A. Jones, T. W. Eagar, and J. H. Lang, J. Phys. D: Appl. Phys. **31**, 107 (1998).
[12]P. Zhu, J. J. Lowke, and R. Morrow, J. Phys. D: Appl. Phys. **25**, 1221 (1992).
[13]J. Haidar, J. Appl. Phys. **84**, 3518 (1998).
[14]J. Haidar and J. J. Lowke, J. Appl. Phys. D: Appl. Phys. **29**, 2951 (1996).
[15]J. Haidar, J. Phys. D: Appl. Phys. **31**, 1233 (1998).
[16]J. Haidar, J. Appl. Phys. **84**, 3530 (1998).
[17]J. Haidar, J. Appl. Phys. **85**, 3448 (1999).
[18]F. L. Zhu, H. L. Tsai, S. P. Marin, and P. C. Wang, Prog. Comput. Fluid Dyn. **4**, 99 (2004).
[19]H. G. Fan and R. Kovacevic, J. Phys. D: Appl. Phys. **37**, 2531 (2004).
[20]J. Hu and H. L. Tsai, Int. J. Heat Mass Transfer **50**, 833 (2007).
[21]J. Hu and H. L. Tsai, Int. J. Heat Mass Transfer **50**, 808 (2007).
[22]V. A. Nemchinsky, J. Phys. D: Appl. Phys. **29**, 1202 (1996).
[23]J. Haidar and J. J. Lowke, IEEE Trans. Plasma Sci. **25**, 931 (1997).
[24]P. G. Jönsson, T. W. Eagar, and J. Szekely, Metall. Trans. B **26**(2), 383 (1995).
[25]J. J. Lowke, R. Morrow, and J. Haidar, J. Phys. D: Appl. Phys. **30**, 2033 (1997).
[26]J. J. Lowke, P. Kovitya, and H. P. Schmidt, J. Phys. D: Appl. Phys. **25**, 1600 (1992).
[27]Q. Z. Diao and H. L. Tsai, Metall. Trans. A **24**(4), 963 (1993).
[28]M. D. Torrey, L. D. Cloutman, R. C. Mjolsness, and C. W. Hirt, Los Alamos Report No. LA-10612-MS, 1985.
[29]J. U. Brackbill, D. B. Kothe, and C. Zemach, J. Comput. Phys. **100**, 335 (1992).
[30]A. Celic and G. G. Zilliac, NASA Technical Report No. 19980137652-A-98-10955, 1998.
[31]S. V. Patanka, *Numerical Heat Transfer and Fluid Flow* (McGraw-Hill,

New York, 1980).
[32]J. F. Lancaster, *The Physics of Welding*, 2nd ed. (Pergamon, Oxford, 1986).
[33]J. Aubreton, M. F. Elchinger, V. Rat, and P. Fauchais, J. Phys. D: Appl-.Phys. **37**, 34 (2004).
[34]W. J. Lick and H. W. Emmons, *Thermodynamic Properties of Helium to 50000 K* (Harvard University Press, Cambridge, MA, 1962).
[35]W. J. Lick and H. W. Emmons, *Transport Properties of Helium from 200 to 50000 K* (Harvard University Press, Cambridge, MA, 1962).
[36]J. Hu and H. L. Tsai, ASME J. Heat Transfer **129**, 1025 (2007).